Supplementary Information

Metal chelating membrane derived TM/TMOₓ nitrogen-doped carbon fibers as efficient oxygen reduction electrocatalyst

Xiaofen Wang,[a,b] Wen Hu,*[a] Jianwei Zhu[a] and Rusen Yang*[a]

[a]School of Advanced Materials and Nanotechnology, Xidian University, Xi'an 710126, P.R. China. E-mail: huwen@xidian.edu.cn, rsyang@xidian.edu.cn

[b]College of Coal and Chemical Industry, Shaanxi Energy Institute, Xianyang 712000, P.R. China.

Experimental Details

Catalysts preparation: Preparation of AO-PAN/CL blend fibrous membrane. Polyarcylonitrile (PAN, $M_w \sim 150000$ g/mol, Sigma-Aldrich) and cellulose acetate (CA, $M_w \sim 30000$ g/mol, Sigma-Aldrich) in a mass ratio of 7:3 were dissolved in N,N-dimethylformamide (DMF, Sinopharm Chemical Reagent Co., Ltd.) at 40°C. Subsequently, the solution was filled in a 10 mL plastic syringe having a 0.4 mm inner diameter stainless-steel needle with 90° blunt end. Grounded counter electrode was connected to a roller covered with aluminum foil as collector. During electrospinning, a positive DC voltage of 16.5 kV was applied to the needle that was placed 20 cm above the collector surface, and the solution feed rate was controlled to be 0.5 mL/h. The optimum mass fraction of PAN plus CA in solution is 13 wt% for electrospinning (Fig. S1). The as-electrospun PAN/CA blend fibrous mat was peeled off from the aluminum foil and dried under vacuum at 60°C for 12 h. Then the PAN/CA blend fibrous mat was deacetylated by immersion in 0.05 M NaOH ethanol/water solution (mass ratio of 1:4) for 24 h at room temperature. After washing and drying, the PAN/regenerated cellulose (PAN/CL) blend fibFrous membrane was obtained. Finally, the amidoxime-modified PAN/CL (AO-PAN/CL) blend fibrous membrane was prepared through the reaction of PAN/CL membrane in 0.15 M hydroxylamine hydrochloride ($NH_2OH \cdot HCl$, Sinopharm Chemical Reagent Co., Ltd.) aqueous solution at pH = 7 under 65°C for 2 h.

Preparation of TM/TMO$_x$@N-CFs from the metal chelating membrane. The $Fe(NO_3)_3 \cdot 9H_2O$, $Co(NO_3)_2 \cdot 6H_2O$, $Ni(NO_3)_2 \cdot 6H_2O$, $Mn(NO_3)_2 \cdot 4H_2O$ (Aladdin Reagent) with 50 mM concentration was dissolved in water respectively. A piece of AO-PAN/CL membrane was immersed in each metal ion solution at room temperature for 24 h. After rinsed with water and drying, the obtained metal chelating membrane was pyrolyzed under N_2 flow at a rate of 5°C min^{-1} up to 900°C for 2 h to get the self-supported TM/TMO$_x$@N-CFs fibers.

Material characterizations: The crystallographic structure and morphology were characterized by XRD (D8 Advance, Bruker, with Cu Kα radiation), optical microscope (LV100ND, Nikon), FE-SEM (Apreo HiVac, FEI) and TEM equipped with EDX (JEM-

2100F, JEOL). The chemical structure was studied using ATR-FTIR spectroscopy (Nicolet iS 50, Thermo Fisher) and Raman spectroscopy (inVia, Renishaw). N_2 sorption analysis was conducted on Autosorb-iQ instrument (Quantachrome). The elemental analysis was carried out using XPS spectroscopy (Thermo Scientific K-Alpha, Thermo Fisher). Elemental Fe loading in bulk Fe/Fe_3O_4@N-CFs sample was determined by Inductively Coupled Plasma-Atomic Emission Spectrometer (ICP-AES, PerkinElmer, Avio 200).

Electrochemical measurements: The catalyst ink was prepared by homogeneously dispersing 5.6 mg samples in 1 mL solution containing 0.1 mL Nafion (5 wt%, Sigma-Aldrich), 0.1 mL isopropanol, and 0.8 mL water. 8.8 μL ink was pipetted on a glassy carbon (GC, 3 mm in diameter) rotating disk electrode (RDE) with a catalyst loading of 0.7 mg cm^{-2}. A 20 wt% Pt/C (Alfa Aesar) catalyst was modified on GC-RDE using the same procedure but with 20 μL Nafion and 0.1 mg cm^{-2} loading (20 μg Pt cm^{-2}). The electrochemical measurements were carried out on Potentiostat/Galvanostat (PARSTAT 4000A and VersaSTAT 3, Princeton Applied Research) equipped with a rotating ring disk electrode apparatus (RRDE-3A, ALS Co., Ltd). The electrocatalytic activities of samples were measured in a conventional three-electrode cell in 0.1 M KOH, 0.1 M PBS and 0.1 M $HClO_4$ electrolyte, respectively. Pt wire (0.5 mm in diameter, ALS Co., Ltd) was used as the counter electrode. Hg/Hg_2Cl_2 electrode was used as the reference electrode in alkaline electrolyte, while Ag/AgCl electrode was used as the reference electrode in neutral and acidic electrolytes. The potentials were normalized to the reversible hydrogen electrode (RHE) using the Nernst equation:

$$E_{\text{RHE}} = E_{\text{Hg/Hg}_2\text{Cl}_2} + 1.0093 \tag{1}$$

$$E_{\text{RHE}} = E_{\text{Ag/AgCl}} + 0.195 + 0.0591 \times \text{pH} \tag{2}$$

Cyclic voltammetry (CV) experiments were performed in N_2/O_2-saturated electrolyte at 50 mV s^{-1}. Linear sweep voltammetry (LSV) measurements were performed in O_2 saturated electrolyte at 10 mV s^{-1} under various rotation rates. In order to evaluate the catalyst stability, chronoamperometry was applied at 0.6 V with a rotation speed of 1600 rpm, and accelerated durability test (ADT) was also performed

for 5000 potential cycles between 0.6-1.0 V at 100 mV s^{-1}. The methanol tolerance was examined by recording the chronoamperometric response with 2 M methanol injection into 0.1 M KOH electrolyte at around 600 s. The electron transfer number during ORR can be calculated using Koutechy-Levich (K-L) equation:

$$\frac{1}{J} = \frac{1}{J_L} + \frac{1}{J_K} = \frac{1}{B\omega^{1/2}} + \frac{1}{J_K} \tag{3}$$

$$B = 0.2nFC_{O_2}D_{O_2}^{2/3}v^{-1/6} \tag{4}$$

wherein J, J_L and J_K represent the measured, diffusion-limiting and kinetic current density, respectively, ω is the electrode rotating speed in rpm, n is the electron transfer number, F is the Faraday constant (96485 C mol^{-1}), C_{O_2} is the saturated O_2 concentration (1.2×10^{-3} mol L^{-1} in 0.1 M KOH), D_{O_2} is the diffusion coefficient of O_2 (1.9×10^{-5} cm^2 s^{-1} in 0.1 M KOH), and v is the kinetic viscosity (0.01 cm^2 s^{-1} for 0.1 M KOH). The constant 0.2 is adopted when the rotating speed is in rpm.

RRDE measurements were tested by LSV in O_2 saturated 0.1 M KOH electrolyte at 10 mV s^{-1} under 1600 rpm, and the Pt ring potential was set at 1.5 V vs. RHE. The yield of peroxide released during ORR (H_2O_2 (%)) and the electron transfer number (n) can be calculated by the following equations:

$$H_2O_2(\%) = \frac{200I_R}{I_R + I_D N} \tag{5}$$

$$n = \frac{4I_D}{I_D + \frac{I_R}{N}} \tag{6}$$

wherein I_R and I_D represent the ring and disk current, respectively, and $N = 0.43$ is the Pt ring current collection efficiency provided by the manufacturer. The GC disk electrode on RRDE (ALS Co., Ltd) is 4 mm in diameter, while the Pt ring electrode on RRDE is 7 mm in outer diameter and 5 mm in inner diameter.

Zn-air batteries tests: The electrocatalyst ink was pipetted onto 1 cm^2 area of PTFE-treated hydrophobic carbon paper to achieve a catalyst loading of 1 mg cm^{-2}. Then the air cathode was prepared by pressing the catalyst-coated carbon paper with nickel foam as the gas diffusion layer. The Pt/C air electrode was prepared with same loading. Zn-

air battery was assembled with the above air cathode, Zn foil (0.2 mm in thickness) as anode and a mixed solution of 6 M KOH and 0.2 M zinc acetate as the electrolyte. The LAND-CT2001A instruments were used to acquire the galvanostatic discharge curves of batteries at various current densities. The open-circuit voltages and the voltage-current polarization data were performed on VersaSTAT 3 instrument. The electrochemical impedance spectroscopy (EIS) measurements were taken over at open-circuit voltage in a frequency range of 0.1 MHz to 10 mHz with an AC amplitude of 5 mV using PARSTAT 4000A. All Zn-air batteries tests were performed under ambient atmosphere at room temperature. The power density (P) was calculated from the discharge polarization profiles using the following equation:

$$P = U \times J \tag{7}$$

wherein U is the discharge voltage, and J is the discharge current density.
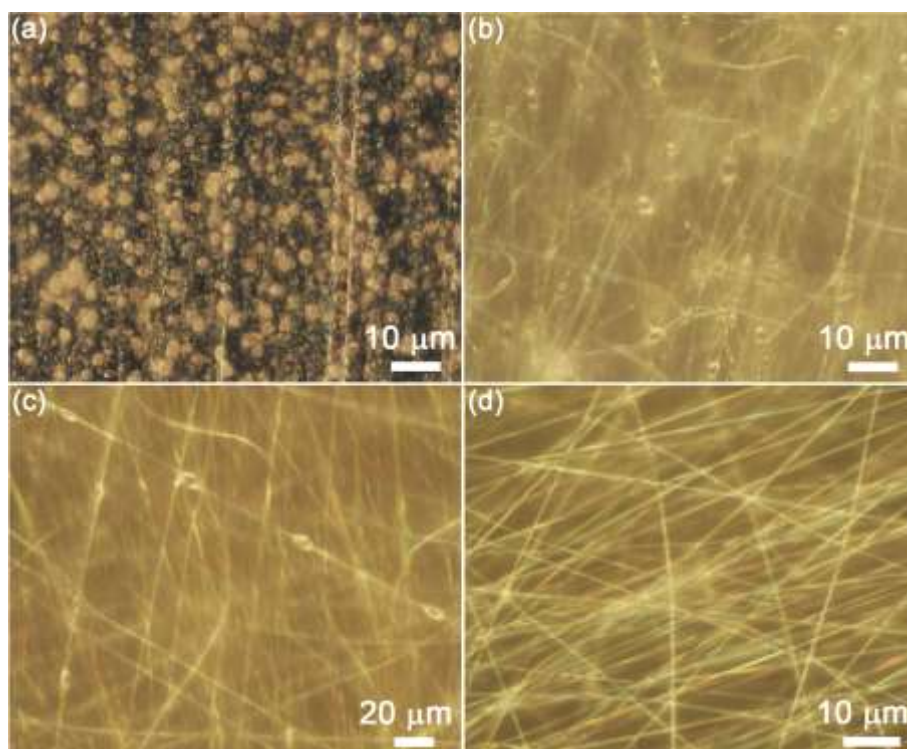
Fig. S1 Optical microscope images of electrospun PAN/CA blend membranes from DMF mixed solutions with various mass fractions of PAN plus CA: (a) 8 wt%, (b) 10 wt%, (c) 12 wt% and (d) 13 wt%.

The mass fraction of PAN plus CA in DMF solution is critical for the continuous fiber formation during electrospinning. From Fig. S1a, if the mass fraction of PAN plus CA is lower than 8 wt%, fibers cannot be generated. When the concentration is increased to 10 wt%, the membrane appeared to contain many large beads on loosely packed fibers (Fig. S1b). At 12 wt% concentration, the mixed solution supported continuous electrospinning, but still a few large and elongated beads can be observed interconnecting with much finer fibers (Fig. S1c). As shown in Fig. S1d, electrospinning of 13 wt% PAN and CA solution can produce continuous fibers with very smooth surfaces and uniform diameters.
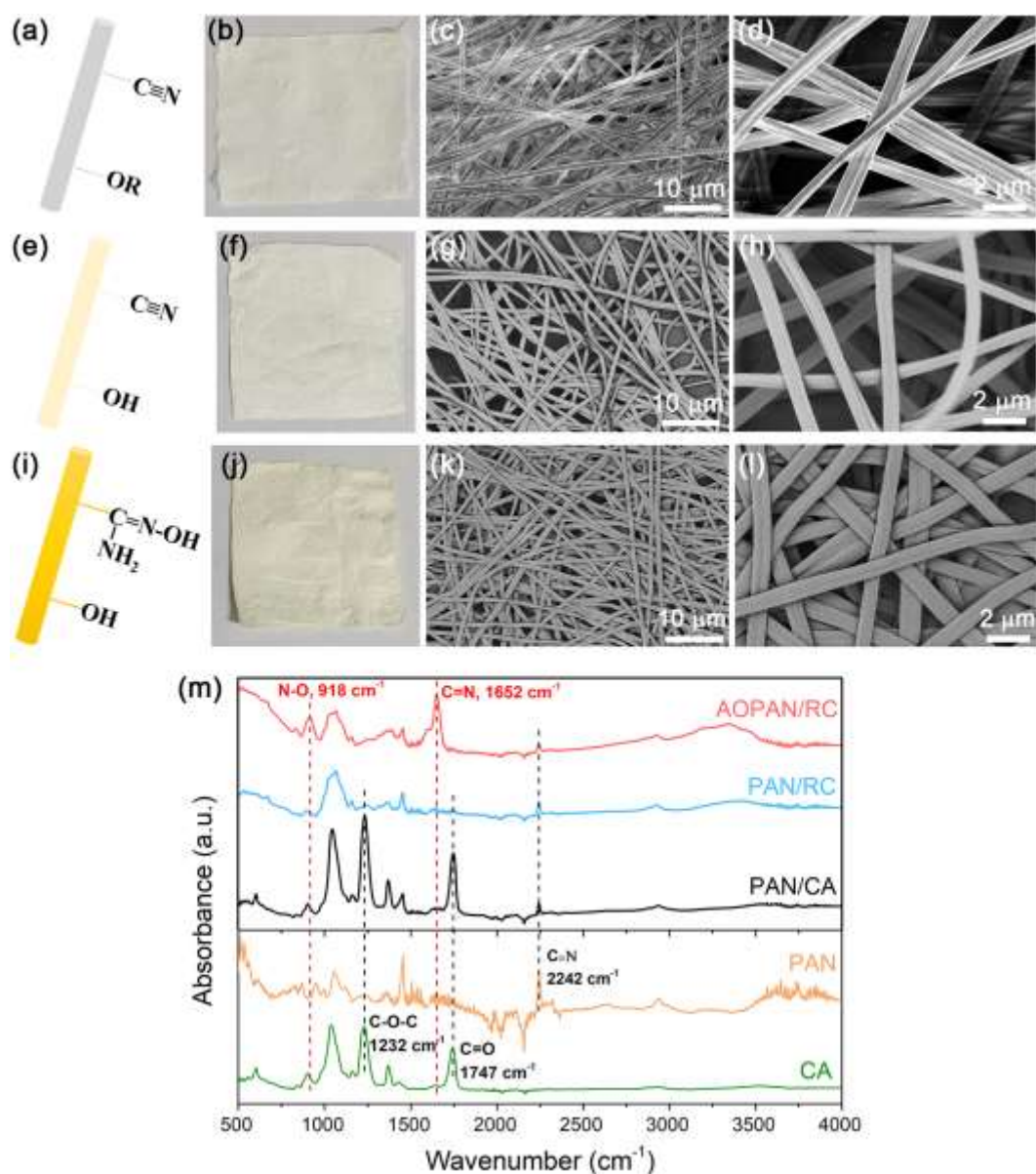
Fig. S2 (a) Chemical structure illustration, (b) photograph and (c,d) FE-SEM images of PAN/CA blend fibrous membrane. (e) Chemical structure illustration, (f) photograph and (g,h) FE-SEM images of PAN/CL blend fibrous membrane. (i) Chemical structure illustration, (j) photograph and (k,l) FE-SEM images of AO-PAN/CL blend fibrous membrane. (m) ATR-FTIR spectra acquired from membranes of CA, PAN, PAN/CA, PAN/CL and AO-PAN/CL.

As shown in Fig. S2a-d, the electrospun PAN/CA blend membrane consists of fibers (400-600 nm in diameter) that are overlaid with an interconnected network structure. Meanwhile, all of the characteristic adsorption peaks of PAN (2242 cm^{-1} corresponding

to C≡N stretching) and CA (1747 cm^{-1} of C=O group, 1232 cm^{-1} of C-O-C group) can be identified in the ATR-FTIR spectrum (Fig. S2m). After basic hydrolysis, the signals of acetyl group disappear, indicating that the CA component in PAN/CA is readily converted into CL. The resulting PAN/CL membrane (Fig. S2e-h) was further reacted with hydroxylamine hydrochloride, then the acquired ATR-FTIR spectrum shows two newly emerged peaks at 1652 and 918 cm^{-1} representing the C=N and N-O groups, respectively, additionally the peak at 2242 cm^{-1} of C≡N stretching is substantially weakened, which clearly indicates that the —C≡N groups of PAN on the fiber surface are converted into —C(NH$_2$)=N-OH amidoxime groups (Fig. S2i-l).
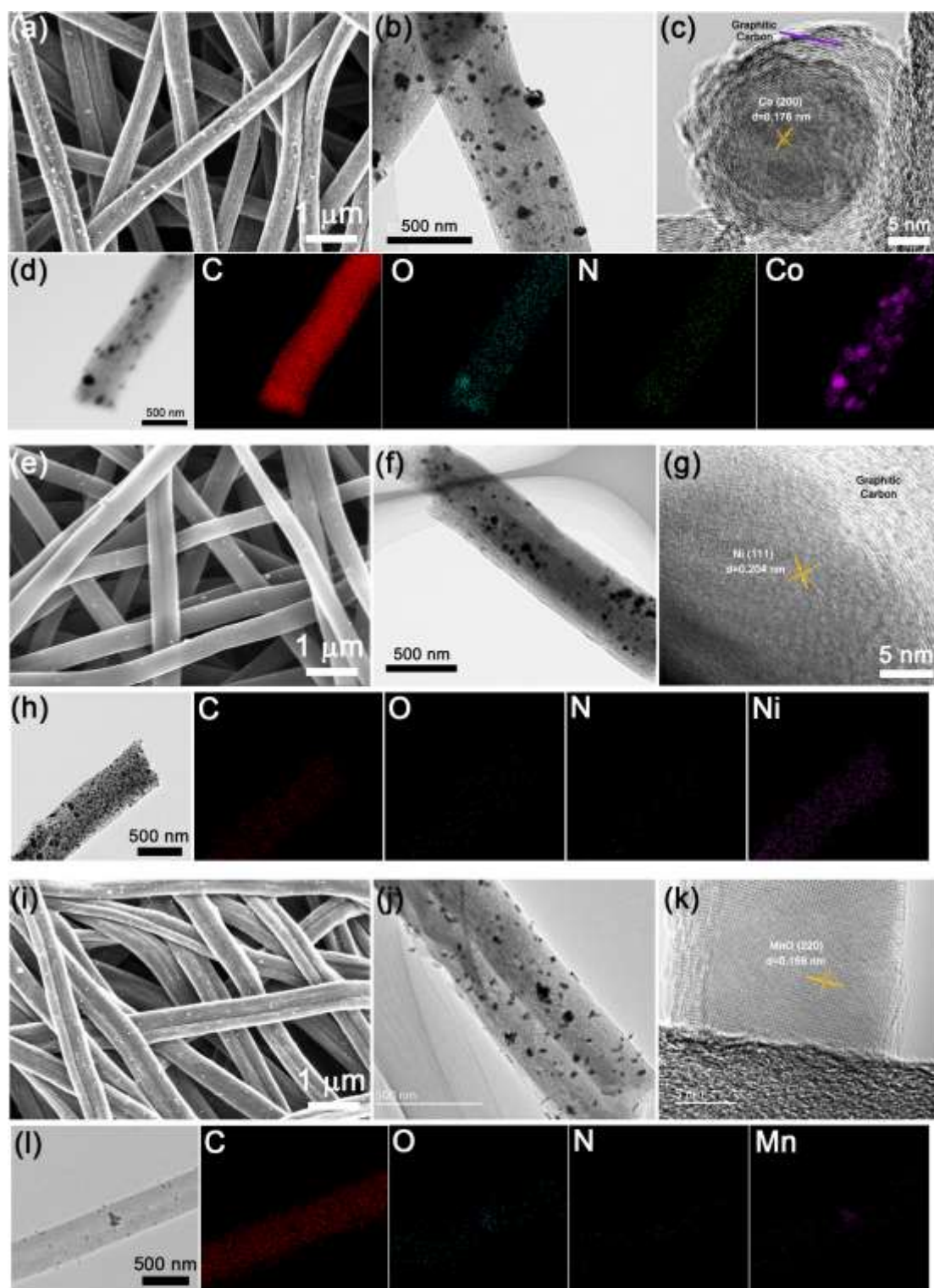
Fig. S3 (a) FE-SEM, (b) TEM, (c) HRTEM images and (d) EDX elemental mapping of Co@N-CFs. (e) FE-SEM, (f) TEM, (g) HRTEM images and (h) EDX elemental mapping of Ni@N-CFs. (i) FE-SEM, (j) TEM, (k) HRTEM images and (l) EDX elemental mapping of MnO@N-CFs.
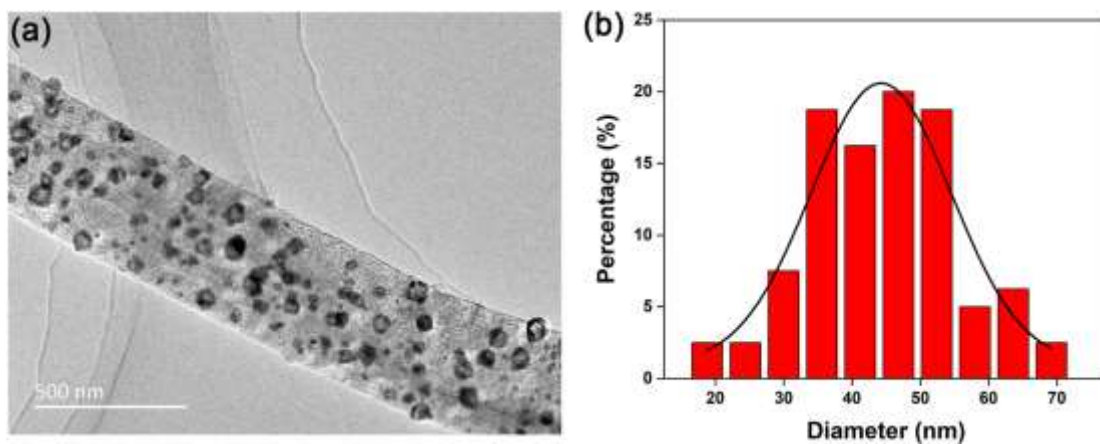
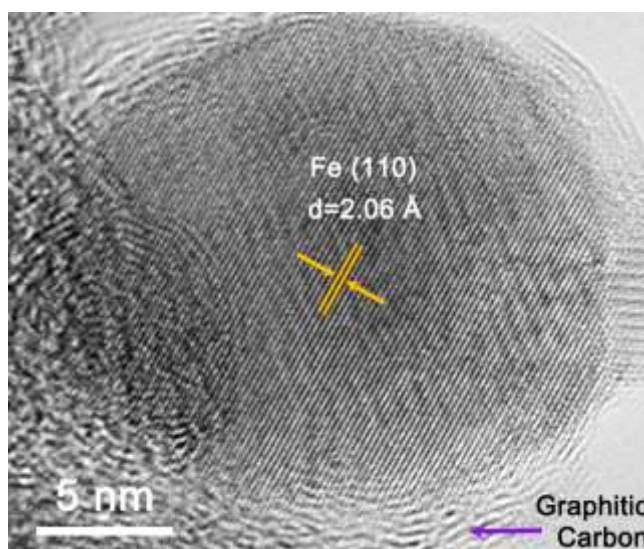**Fig. S4** (a) TEM image of Fe/Fe$_3$O$_4$@N-CFs and (b) corresponding particle size distribution of Fe$_3$O$_4$ nanoparticles.

Fig. S5 HRTEM image of Fe nanoparticle in Fe/Fe$_3$O$_4$@N-CFs.
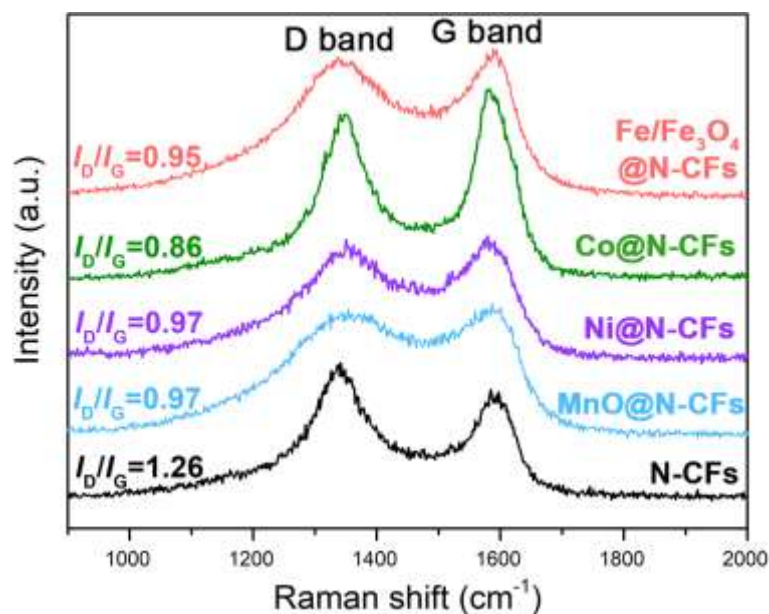
Fig. S6 Raman spectra of TM/TMO$_x$@N-CFs and N-CFs.
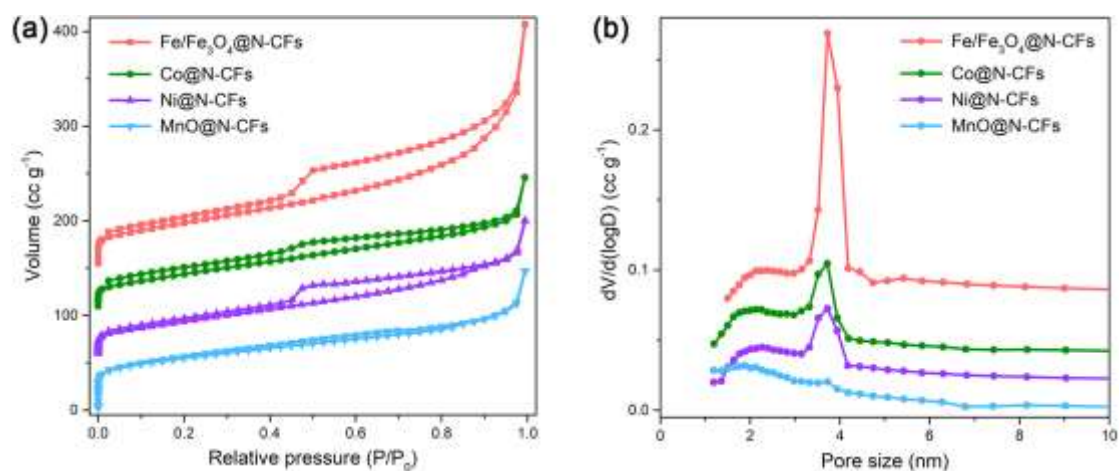

Fig. S7 (a) Nitrogen sorption isotherms and (b) pore size distributions of TM/TMO$_x$@N-CFs.

The Brunauer-Emmett-Teller (BET) specific surface area of Fe/Fe$_3$O$_4$@N-CFs, Co@N-CFs, Ni@N-CFs and MnO@N-CFs are 183.6, 149.9, 139.8 and 183.2 m^2 g^{-1}, respectively.
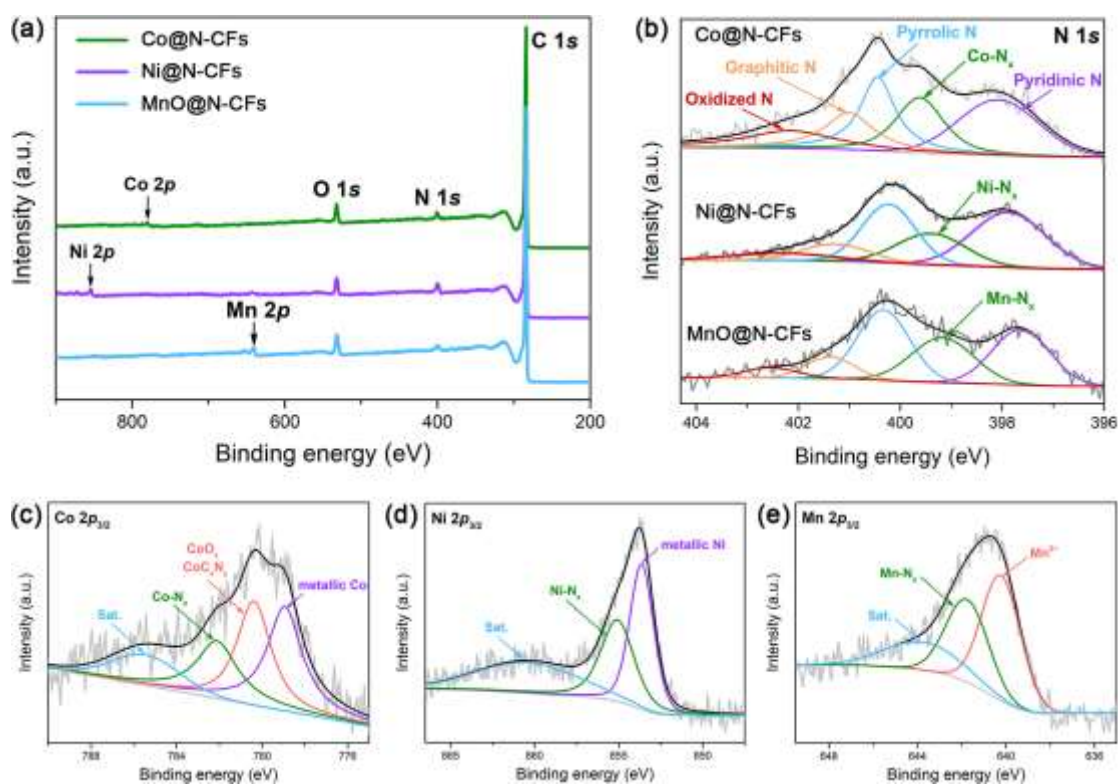
Fig. S8 (a) XPS survey spectra, and high resolution (b) N 1s, (c) Co 2$p_{3/2}$, (d) Ni 2$p_{3/2}$, (e) Mn 2$p_{3/2}$ spectra of Co@N-CFs, Ni@N-CFs and MnO@N-CFs, respectively.

For Co@N-CFs, the full XPS spectrum shows peaks of C 1s, N 1s, O 1s, and Co 2p. The N 1s XPS spectrum reveals five types of nitrogen species, assigned to pyridinic N (398.1 eV, 26.7%), Co-N$_x$ (399.6 eV, 20.1%), pyrrolic N (400.4 eV, 23.1%), graphitic N (401.0 eV, 16.1%) and oxidized N (402.1 eV, 14.0%), respectively. The Co 2$p_{3/2}$ spectrum includes four subpeaks which are ascribed to metallic Co (778.9 eV), CoO$_x$ or CoC$_x$N$_y$ (780.4 eV), Co-N$_x$ (782.1 eV), and the satellite (785.4 eV), respectively.

For Ni@N-CFs, the XPS survey scan confirms the presence of C, N, O and Ni. The N 1s XPS spectrum matches with pyridinic N (397.9 eV, 36.6%), Ni-N$_x$ (399.5 eV, 19.1%), pyrrolic N (400.3 eV, 28.0%), graphitic N (401.4 eV, 10.1%) and oxidized N (402.4 eV, 6.2%), respectively. The Ni 2$p_{3/2}$ spectrum splits into metallic Ni, Ni-N$_x$ and satellite peak at about 853.6, 855.1 and 860.8 eV, respectively.

For MnO@N-CFs, the XPS survey scan shows the presence of C, N, O and Mn. The N 1s XPS spectrum can be fitted by five types of N doping configurations: pyridinic

N (397.6 eV, 28.6%), Mn-N$_x$ (399.2 eV, 24.9%), pyrrolic N (400.3 eV, 32.6%), graphitic N (401.4 eV, 9.2%) and oxidized N (402.5 eV, 4.7%), respectively. The Mn $2p_{3/2}$ spectrum displays the binding energies of Mn^{2+} (640.2 eV) and Mn-N$_x$ (641.7 eV) along with a satellite peak at 643.7 eV.
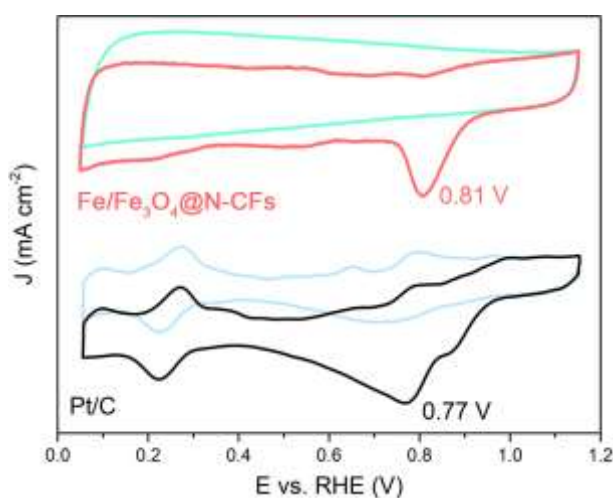

Fig. S9 CV curves of Fe/Fe$_3$O$_4$@N-CFs and Pt/C electrocatalysts in O$_2$/N$_2$-saturated 0.1 M KOH at 50 mV s^{-1}.

The CV curve of Fe/Fe$_3$O$_4$@N-CFs collected in N$_2$-saturated KOH solution does not appear any redox behavior. In contrast, when the electrolyte is saturated with O$_2$, a well-defined oxygen reduction peak centered at 0.81 V is present, which is more positive than Pt/C (0.77 V), demonstrating that the ORR activity of Fe/Fe$_3$O$_4$@N-CFs is superior to Pt/C.
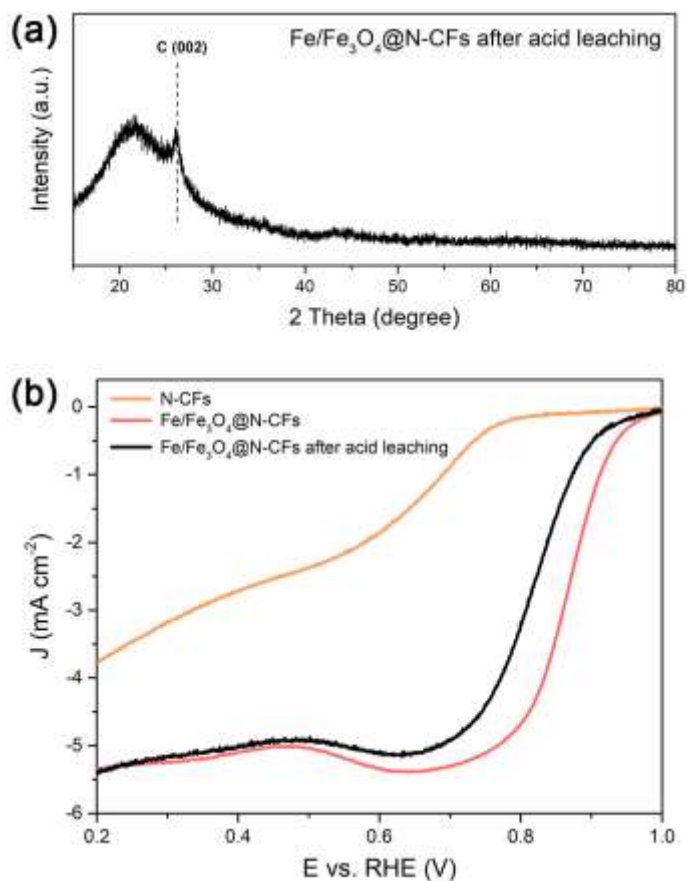
Fig. S10 (a) XRD pattern of Fe/Fe₃O₄@N-CFs after acid leaching. (b) LSV curves of Fe/Fe₃O₄@N-CFs, Fe/Fe₃O₄@N-CFs after acid leaching and N-CFs catalysts in O_2-saturated alkaline electrolyte at 1600 rpm and 10 mV s⁻¹.

In order to reveal which is the main active site among Fe/Fe₃O₄ nanoparticles, N-C and Fe-N$_x$ in our case, the as-obtained Fe/Fe₃O₄@N-CFs was treated in 0.2 M HCl for 4 h at room temperature. From the XRD result shown in Fig. S10a, there are no distinct diffraction peaks of Fe₃O₄ and Fe anymore, demonstrating that the Fe/Fe₃O₄ nanoparticles have been successfully etched away. Then the ORR activities of Fe/Fe₃O₄@N-CFs after acid leaching is compared with Fe/Fe₃O₄@N-CFs and N-CFs by LSV. As shown in Fig. S10b, both the onset potential and half-wave potential of Fe/Fe₃O₄@N-CFs after acid leaching ($E_{onset} = 0.948$ V, $E_{1/2} = 0.816$ V) are lower than Fe/Fe₃O₄@N-CFs ($E_{onset} = 0.985$ V, $E_{1/2} = 0.867$ V), but much higher than N-CFs ($E_{onset} = 0.798$ V, $E_{1/2} = 0.605$ V). Therefore, both Fe-N$_x$ and Fe/Fe₃O₄ nanoparticles are supposed to be the main active sites, and the Fe/Fe₃O₄ nanoparticles play the most crucial role in the ORR activity of Fe/Fe₃O₄@N-CFs.
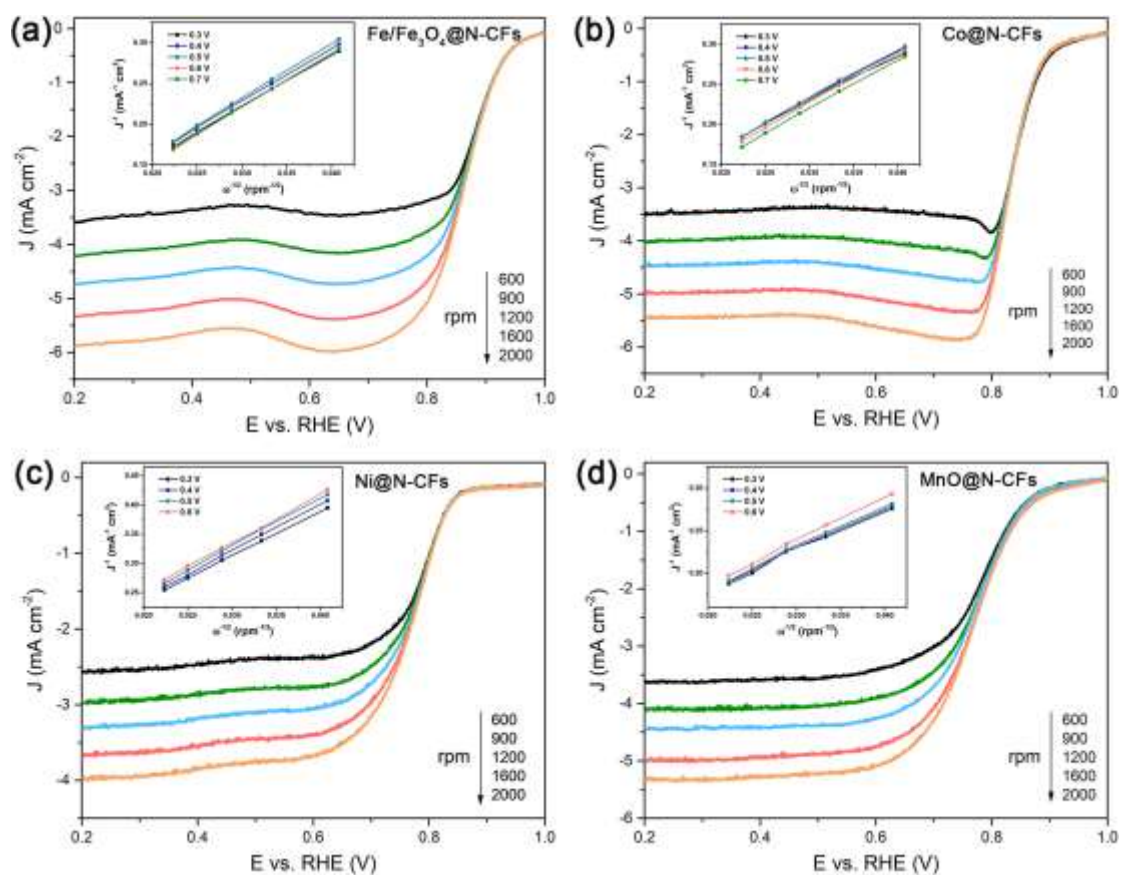
Fig. S11 LSV curves of (a) Fe/Fe₃O₄@N-CFs, (b) Co@N-CFs, (c) Ni@N-CFs and (d) MnO@N-CFs at different rotating speeds, the inset figure are their K-L plots at various electrode potentials, respectively.
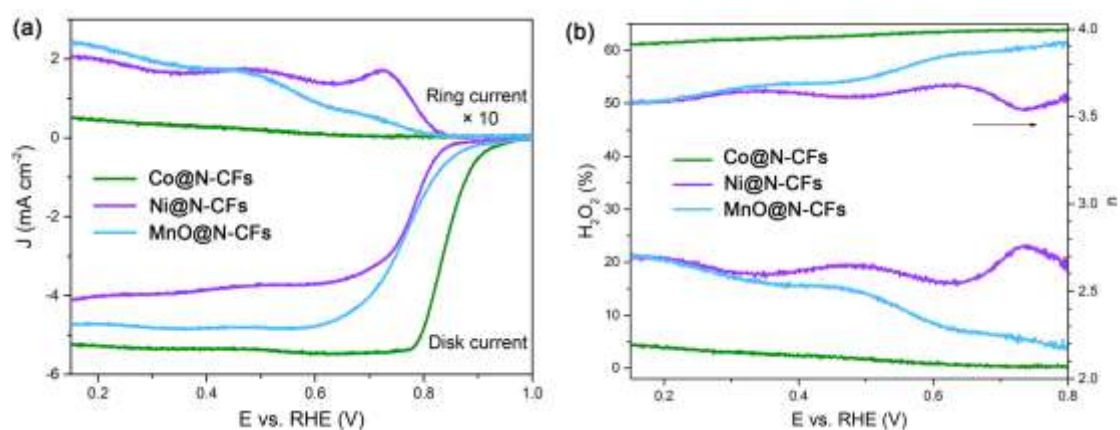

Fig. S12 (a) RRDE voltammograms, and the derived (b) H₂O₂ yield and electron transfer number of Co@N-CFs, Ni@N-CFs and MnO@N-CFs.
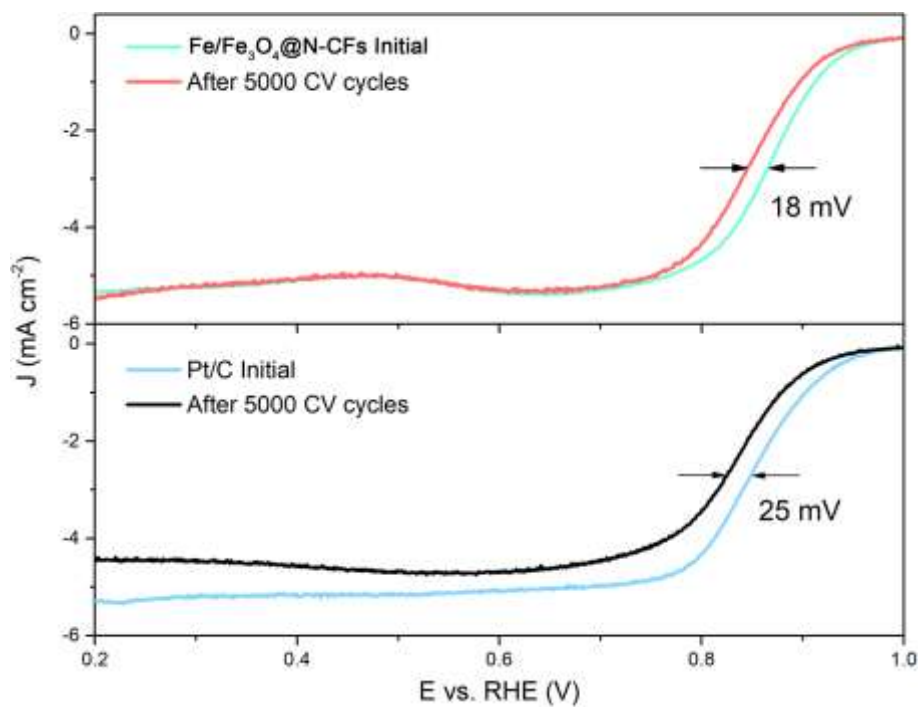
Fig. S13 LSV curves of Fe/Fe$_3$O$_4$@N-CFs and Pt/C after ADT tests.
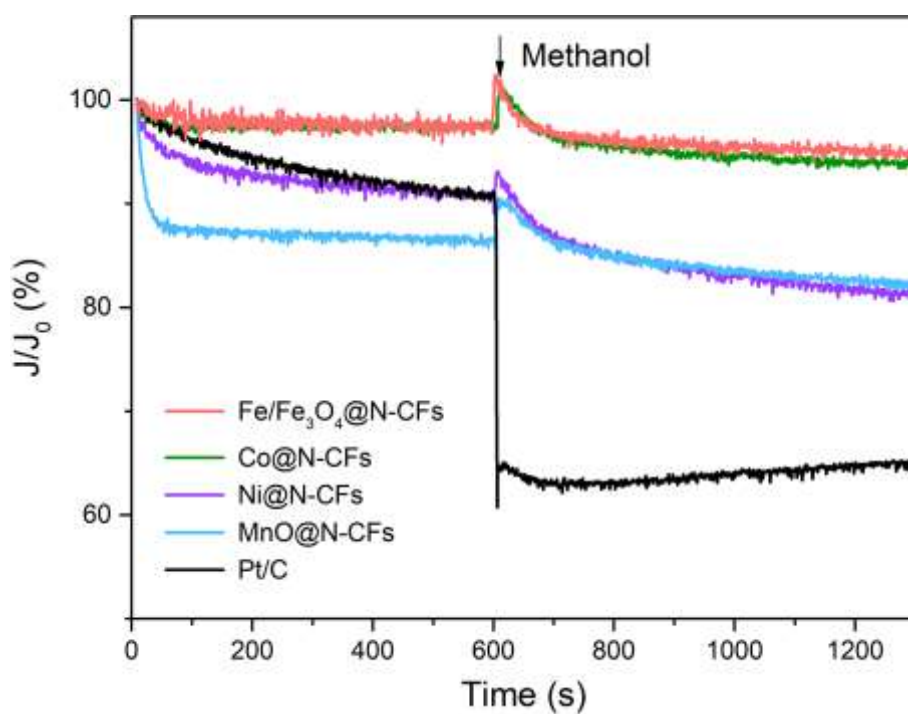

Fig. S14 Normalized *i-t* chronoamperometric responses of various TM/TMO$_x$@N-CFs and Pt/C at 0.6 V and 1600 rpm with methanol addition at around 600 s.
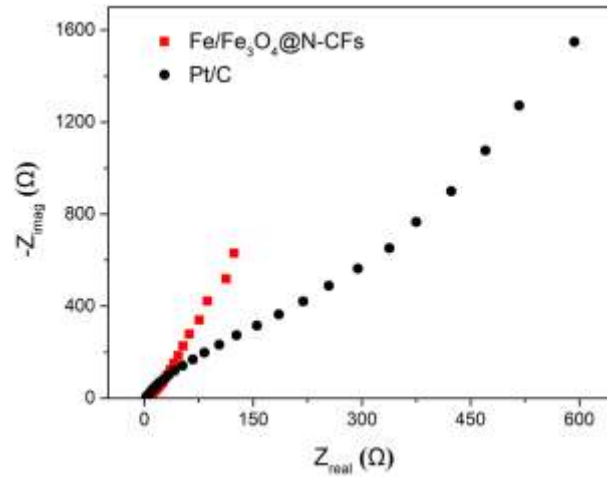
Fig. S15 Typical Nyquist plots of Zn-air batteries with Fe/Fe$_3$O$_4$@N-CFs and Pt/C as air cathodes.

The Fe/Fe$_3$O$_4$@N-CFs-based battery shows smaller charge transfer resistance at high frequency region and better OH$^-$ diffusion behavior at low frequency region than Pt/C, indicating that Fe/Fe$_3$O$_4$@N-CFs possess superior electrical conductivity and excellent mass transfer ability owing to the high graphitization degree and 3D interconnected open pore structure provided by its N-CFs framework.
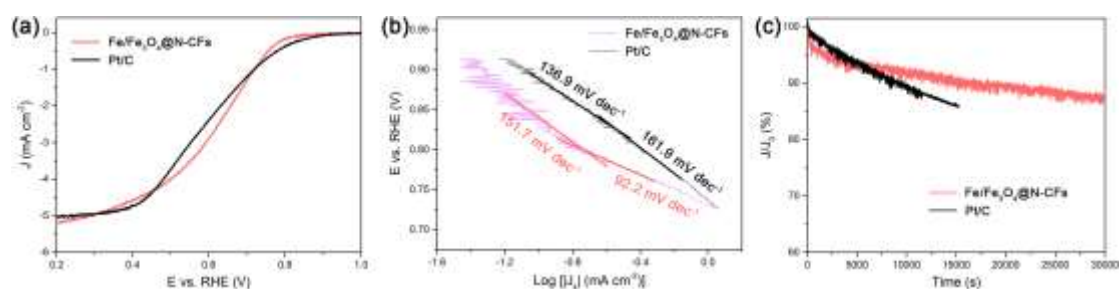
Fig. S16 (a) LSV curves, (b) Tafel plots and (c) chronoamperometry curves of Fe/Fe$_3$O$_4$@N-CFs and Pt/C in O$_2$-saturated 0.1 M PBS electrolyte.

According to the LSV curves (Fig. S16a), the E_{onset} value of Fe/Fe$_3$O$_4$@N-CFs (0.833 V) is slightly negative than Pt/C (0.876 V). However, in the following mixed control region, the current densities of Fe/Fe$_3$O$_4$@N-CFs rapidly increase with $E_{1/2}$ of 0.618 V, higher than Pt/C (0.583 V). The enhanced ORR activity of Fe/Fe$_3$O$_4$@N-CFs is further confirmed by its two-step Tafel slope (Fig. S16b), which shifts from 151.7 mV dec^{-1} to 92.2 mV dec^{-1} with increasing overpotential. The Pt/C electrocatalyst also exhibits a potential-dependent Tafel slope in O$_2$-saturated 0.1 M PBS electrolyte, but the value increases from 136.9 mV dec^{-1} to 161.9 mV dec^{-1}. As for the durability evaluation, Fe/Fe$_3$O$_4$@N-CFs remains 87% of the initial current after 30000 s chronoamperometric measurements (Fig. S16c), while Pt/C fades 14% of its initial current only after 15000 s chronoamperometric tests, demonstrating that Fe/Fe$_3$O$_4$@N-CFs manifests superb stability also in neutral medium.

Table S1 Comparison of Zn-air battery performances with Fe/Fe$_3$O$_4$@N-CFs and other recently reported TM/TMO$_x$ based air cathodes.

Electrocatalyst	Open Circuit Voltage (V)	Peak Power Density (mW cm^{-2})	Specific Capacity (mAh g$_{Zn}^{-1}$)	Reference
Co/CoO$_x$-N-C	1.443	—	610	Appl. Surf. Sci. 2018, 456, 959
Ni-MnO/rGO aerogels	—	123	758	Adv. Mater. 2018, 30, 1704609
2D-Fe$_3$O$_4$@FeNC-700	1.433	138	796	Chem. Commun. 2019, 55, 7538
Fe$_3$O$_4$@ oxygen vacancy N-C	—	106	724	J. Colloid Interf. Sci. 2020, 567, 410
Fe-Ni@N,S-C aerogel	—	140.3	750.7	Small 2021, 17, 2102002
Ni-MnO/N-C	1.446	179.2	702	J. Power Sources 2021, 485, 229330
Co-NC-800	1.44	105.3	657.2	Chem. Eng. J. 2021, 409, 128171
Fe$_3$O$_4$/Fe$_2$O$_3$/Fe@NC	1.54	106.8	800.1	J. Mater. Chem. A, 2021, 9, 2764
Co/MnO@N,S-CNT/CNFs	1.45	120.7	726.6	Appl. Catal. B-Environ. 2021, 295, 120281
Ni-doped Mn$_2$O$_3$	1.52	88.2	813.5	Int. J. Hydrogen Energy. 2022, 47, 2378
MnNC	1.46	130	819	ACS Sustainable Chem. Eng. 2022, 10, 224
FeNi@N-C	1.48	99.2	802.18	Chem. Eng. J. 2022, 437, 135295
MnO/N-rGO	1.47	146	790	Ceram. Int. 2023, 49, 13972
Ni-SiNC	—	161	748	Small 2023, 19, 2206071
Ni-Co/NC foams	1.44	138	751	J. Power Sources 2023, 571, 233069
FeCo-NC	1.499	77	—	J. Colloid Interf. Sci. 2023, 635, 186
Co@NC nanorods	1.54	76.76	726	Energy Environ Mater 2023, 6, e12389
Fe/Fe$_3$O$_4$@N-CFs	**1.56**	**132.4**	**776.4**	**This work**